SPECIAL
Air-sea interaction during PISTON-MISOBOB-CAMP2Ex
COLLECTION

Evaluating Coupled Climate Model Parameterizations via Skill at Reproducing the Monsoon Intraseasonal Oscillation

PATRICK ORENSTEIN,[a] BAYLOR FOX-KEMPER,[a] LEAH JOHNSON,[a] QING LI,[b] AND AAKASH SANE[c]

[a] *Department of Earth, Environmental, and Planetary Sciences, Brown University, Providence, Rhode Island*
[b] *Thrust of Earth, Ocean and Atmospheric Sciences, The Hong Kong University of Science and Technology (Guangzhou), Nansha, Guangzhou, Guangdong, China*
[c] *School of Engineering, Brown University, Providence, Rhode Island*

(Manuscript received 27 April 2021, in final form 12 December 2021)

ABSTRACT: Empirically generated indices are used to evaluate the skill of a global climate model in representing the monsoon intraseasonal oscillation (MISO). This work adapts the method of Suhas et al., an extended empirical orthogonal function (EEOF) analysis of daily rainfall data with the first orthogonal function indicating MISO strength and phase. This method is applied to observed rainfall and Community Earth System Model (CESM1.2) simulation results. Variants of the CESM1.2 including upper ocean parameterizations for Langmuir turbulence and submesoscale mixed layer eddy restratification are used together with the EEOF analysis to explore sensitivity of the MISO to global upper ocean process representations. The skill with which the model variants recreate the MISO strength and persistence is evaluated versus the observed MISO. While all model versions reproduce the northward rainfall propagation traditionally associated with the MISO, a version including both Langmuir turbulence and submesoscale restratification parameterizations provides the most accurate simulations of the time scale of MISO events.

KEYWORDS: Indian Ocean; Turbulence; Monsoons; Air-sea interaction; Empirical orthogonal functions; Parameterization

1. Introduction

Variability in the Indian monsoon on multiple time scales has been an area of intense research due to its significant societal and economic importance to the subcontinent and Indian Ocean periphery. Variations both from year to year (interannual) and over the course of a single season (intraseasonal/subseasonal) are much harder to predict, and have been a topic of significant interest to researchers (Goswami et al. 2016; Kuppam and Mawsynram 2019). For the purposes of predictive skill, interannual and intraseasonal variability appear to be distinct phenomena, allowing—perhaps requiring—weather models to account for them separately (Krishnamurthy and Shukla 2000).

One primary mode of variability is the Indian monsoon intraseasonal oscillation (MISO), which causes brief periods of especially intense rainfall during the Asian monsoon on the Indian subcontinent and over the Bay of Bengal (BOB). At the most basic level, the MISO is defined as a deviation from the seasonal monsoon rainfall trend, which gradually increases over the course of the summer, peaks around late July, then decreases to its off-season intensity (Krishnamurti and Ardanuy 1980). This is generated in part by the annual north–south movement of the monsoonal intertropical convergence zone (Goswami and Mohan 2001). As a result, MISO events occur in an extremely complex circulation context, making them difficult to predict more than a few weeks in advance (Mo 2001). Nonetheless, they exhibit a northward propagation and some predictability, and they can be isolated using the empirical pattern recognition techniques of Suhas et al. (2013) as shown in Fig. 1. The MISO has significant marine influences and impacts, involving ocean–atmosphere heat and freshwater exchange, and is extremely dependent on the particular geometry and physical characteristics of the BOB (Goswami et al. 2016). Y. Li et al. (2016, 2018) demonstrate important mixed layer–related biases in the simulations of the BOB in the Coupled Forecast System (CFSv2), and speculate that improving mixed layer physical process representation may help. The Indian monsoon is a known source of error in phase 5 of the Coupled Model Intercomparison Project (CMIP5) models (Li et al. 2015).

Previous work has looked at the relationship between the interannual and intraseasonal variations in the Indian monsoon.

Orenstein's current affiliation: Department of Applied Physics and Applied Mathematics, Columbia University, New York, New York.

Johnson's current affiliation: Applied Physics Laboratory, University of Washington, Seattle, Washington.

Sane's current affiliation: Program in Atmospheric and Oceanic Sciences, Princeton University, Princeton, New Jersey.

Corresponding author: Baylor Fox-Kemper, baylor@brown.edu

DOI: 10.1175/JCLI-D-21-0337.1

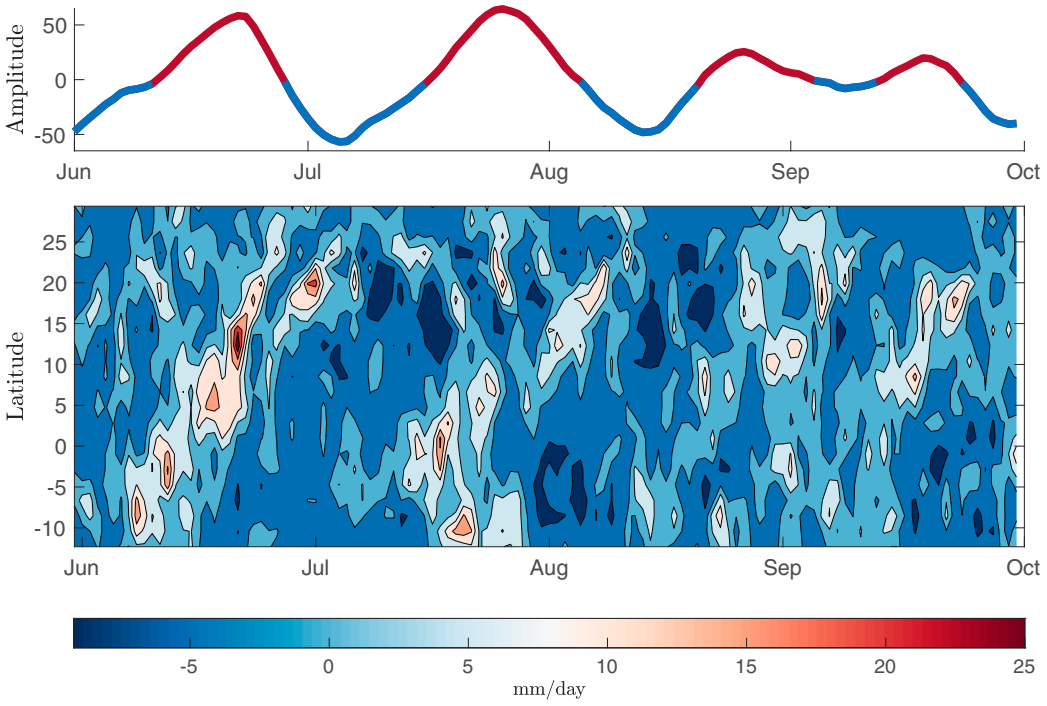

FIG. 1. Example of EEOF index method for summer 2007 observed precipitation. (top) The value of the EEOF1 index over the course of the monsoon season. (bottom) A transposed Hovmöller diagram showing the zonally averaged precipitation anomaly data from that period used in the EEOF method (described in section 2c). Diagonal areas of high precipitation correspond to northward-propagating rainbands, which in turn correspond to periods of positive EEOF1 (portions of the top plot in red).

Goswami and Mohan (2001) found that while the two behaviors act on different time scales, they are not independent phenomena. Since they exhibit similar spatial patterns, the interannual variation in monsoons can be viewed as an anomaly in intraseasonal (i.e., MISO) activity. The authors inferred that the chaotic nature of intraseasonal oscillations therefore spelled defeat for researchers trying to predict year-to-year monsoon trends. Empirical methods offer a way to circumvent this limitation by isolating modes of variation in chaotic data, and here they are extended to use in model evaluation. Through this combination of models and pattern recognition, skill in reproducing the MISO statistics can be assessed, which in turn may be used to improve forecast systems.

Not only are MISOs important to the intensity of the monsoon overall, but positive phases (indicated by red shading of the time series in Fig. 1, top panel) have been shown to be correlated with a greater frequency of tropical cyclones forming in the BOB (Akter and Tsuboki 2014). Moreover, those storms associated with a positive MISO phase tend to form at a central point in the northern BOB and travel northwest across India, steered by the low pressure boundary known as the monsoon trough. This origin point corresponds with the location of greatest MISO variation in the Bay, meaning that variability in the MISO may affect weather events in the region (Goswami et al. 2003).

A key result here is that the connectivity of rainfall over the subcontinent to the MISO variability over the BOB is sensitive to upper ocean physics in a coupled model. The bay is particularly important as MISOs form in the Indian Ocean to the south and move northward, and previous studies have found a zone of peak variation to be centered on the bay (Goswami et al. 2003; Goswami and Xavier 2003; Sengupta et al. 2001).

The Community Earth System Model, version 1.2 (CESM1.2: Hurrell et al. 2013) is a global coupled modeling system. The particular variants being used for this study use the standard atmosphere, sea ice, and land components, but differ in key ocean model parameterizations (Table 1). The goal in studying the MISO in these configurations was to determine if its statistics are sensitive to the upper ocean physics (as shown with less direct attribution to specific upper ocean processes in Y. Li et al. 2016, 2018; Samanta et al. 2018; Zhang et al. 2018), and whether optimization of these physical parameterizations might usefully

TABLE 1. List of CESM case studies used in this study.

	KPP	Langmuir	Submesoscale
CTRL	x	x	x
noLT	x		x
noSM	x	x	
noLTSM	x		

improve skill in coupled forecast systems (e.g., Pattanaik et al. 2012). The specific upper ocean physical processes being evaluated are wave-induced mixing, or Langmuir turbulence, as parameterized by Q. Li et al. (2016) and submesoscale mixed layer eddy restratification as parameterized by Fox-Kemper et al. (2008, 2011). As of CESM1.2 the submesoscale parameterization is standard, but the Langmuir turbulence parameterization, built upon the KPP scheme (Large et al. 1994), was only included as a default setting in CESM2 (Danabasoglu et al. 2020). The CESM1.2 variants being evaluated here are prototypes including both parameterizations that preceded CESM2, but are similar in terms of the ocean model setup.

Recent studies have shown the potential for upper ocean processes to impact the frequency and intensity of the MISO. Zhang et al. (2018) found a quadrature relationship between SST and precipitation in smoothed observations, indicating that these two quantities share a relationship which they posited involves warm SSTs promoting atmospheric convection. This opens up a potential role for SST–and the ocean mixing and restratification processes that affect it—in the phasing of monsoon active cycles. Samanta et al. (2018) showed that imposing a realistic mixed layer depth (MLD) profile in the BOB onto an ocean–atmosphere coupled forecast model improved its skill with respect to SST and rainfall. Therefore it is reasonable to hypothesize that processes that impact the MLD will influence monsoon variability.

Upper ocean mixing in the BOB is set by processes that inhibit mixing, such as buoyancy input from warming and freshwater fluxes, and those that enhance mixing such as wind driven mixing or convection. In addition to surface forcing at the air–sea interface, other processes are known to be leading order determinants of upper ocean turbulence. In particular, this work focuses on the restratifying effects of submesoscale baroclinic instability and enhanced mixing due to Langmuir circulation and turbulence, a variety of mixing that derives some of its energy from surface waves (McWilliams et al. 1997; Li et al. 2019). Submesoscale restratification plays an essential role in the upper ocean buoyancy budget where there are strong horizontal density gradients. Large freshwater input into the BOB from river runoff (e.g., from the Bramaputra River) is stirred into the interior of the bay and creates sharp buoyancy fronts and filaments (MacKinnon et al. 2016; Ramachandran et al. 2018; Spiro Jaeger and Mahadevan 2018; Sarkar et al. 2016). Instabilities that occur at submesoscale fronts act to slump horizontal buoyancy gradients to create vertical stratification and inhibit upper ocean mixing (Boccaletti et al. 2007; Fox-Kemper et al. 2008). Conversely, Langmuir turbulence results from wind–wave interaction, which creates parallel rotating cells $\sim 10^1$ m deep and is known to enhance turbulence in the ocean surface boundary layer (Langmuir 1938; Leibovich 1983; McWilliams et al. 1997; McWilliams and Sullivan 2000; Li et al. 2019). The shoaling/deepening effects of these processes have been parameterized for coarse-resolution models such as global circulation models and coupled weather forecast models that cannot simulate these processes directly.

Previous studies have defined MISOs using a variety of indices, including atmospheric vorticity at 850 hPa (Goswami et al. 2003), zonal wind (Goswami and Mohan 2001), and sea surface temperature at a stationary buoy (Sengupta et al. 2001). These choices reflected authors' assumptions about MISO dynamics; for instance, Goswami and Mohan (2001)'s use of zonal wind in the BOB as a metric reflected their view that MISOs were an expression of breaks in the prevailing monsoon winds.

The methodology presented here is different in two ways. First, it uses rainfall data, meaning MISOs are measured by their effects, not their causes, insulating the analysis from discussions of the mechanisms of individual MISO phases. While increased rainfall alone does not define a MISO, it is a well-established relationship (and the most impactful on human activity). Second, this work expands on the technique of Suhas et al. (2013), using an EEOF analysis to identify the oscillatory signal of the MISO rainfall data. Empirical orthogonal function (EOF) analysis decomposes complex datasets into their primary modes of variability, revealing which geographic and temporal patterns are most significant to the overall variability (Thomson and Emery 2001). This allows spatially stationary oscillatory patterns (e.g., standing waves) to be revealed (Fox-Kemper 2004). EEOF analysis takes this a step further, using in this case multiple snapshots over a short time window as the "pattern" being recognized constructed to reveal propagating modes of variability (Eshel 2012; Weare and Nasstrom 1982). The EEOFs tend to isolate the northward propagation characteristic of the classical MISO phase progression (Suhas et al. 2013).

This work uses an EEOF methodology to isolate MISO events and compare different formulations of upper ocean parameterizations within CESM with observations. The comparison provides insight into how much of a difference upper ocean processes have on MISO events, as well as more generally how well the CESM1.2 simulates the MISO. CESM is a climate rather than a weather forecast model, so the issue of model skill is focused on the model's ability to simulate a realistic MISO with reasonable magnitude and recurrence, rather than its ability to produce good forecasts from observed initial conditions. However, as the National Centers for Environmental Prediction (NCEP) Coupled Forecast System (CFS) that is often used in this region shares significant code and capabilities with CESM, implications for what constitutes a skillful CESM is expected to resemble what constitutes a skillful CFS. To that end, Section 2 lays out the ocean turbulence parameterizations which we evaluate in detail and the details of the EEOF procedure. Section 3 discusses the metrics used to visualize and evaluate the results of the EEOF method, as well as presenting the effect of the parameterizations on other model variables and their similarity to observations. Finally, section 4 considers the significance of these results and what they imply about the model versions.

2. Methods

a. Observational data

Following Suhas et al. (2013), the observational rainfall dataset used for model comparison is the Global Precipitation Climatology Project (GPCP), a reanalysis based on both satellite and historical observations (Huffman et al. 1997; Adler et al. 2003; Huffman et al. 2009). This dataset in $1° \times 1°$

horizontal resolution was obtained for 1 October 1996–30 September 2015, and was then regridded onto the 1.9° × 2.5° resolution of the CESM atmospheric model for comparison.

Additionally, we used MLD climatology data from Montégut et al. (2004), accessed through the French Research Institute for Exploitation of the Sea (IFREMER). The data used here define the MLD using potential temperature, which is more comparable to the MLD definition used in the model output. Specifically, Montégut et al. (2004) defined the bottom of the mixed layer as the depth at which potential temperature θ has decreased by 0.2°C from θ at 10-m depth (meaning the MLD is assumed to always be at least 10 m). SST data for further model comparison are taken from the Group for High Resolution Sea Surface Temperature (GHRSST) global Level 4 sea surface temperature analysis of the National Centers for Environmental Information (NCEI) (Reynolds et al. 2007), which integrates satellite output with observations from moorings and profiling floats.

b. CESM

This work uses the National Center for Atmospheric Research (NCAR) Community Earth System Model, version 1.2 (CESM1.2). Previously, CESMv1 was found to have the smallest bias in simulating the monsoon compared to other CMIP5 models (Anand et al. 2018). The model configuration includes a fully coupled atmosphere (CAM4) and land (CLM4.0) on a 1.9° × 2.5° nominal grid, and ocean (POP2) along with sea ice (CICE4) on the gx1 version 6 grid (1° nominal resolution), and waves (WAVEWATCH III v3.14) on a coarser grid (Q. Li et al. 2016). The model is run for 100 years with steady preindustrial conditions. This analysis uses the last 30 years of integration after which the model is assumed to be sufficiently equilibrated in the upper ocean, as MLDs are stable when different decades at the end of the simulation are compared. Boundary layer turbulence is parameterized using the *K*-profile parameterization (KPP) mixing scheme (Large et al. 1994), and the additional effects of restratification by submesoscale mixed layer eddies (Fox-Kemper et al. 2011) and enhanced vertical mixing through Langmuir turbulence (Q. Li et al. 2016) can be switched on or off. The different simulations for comparison are all forced with the same conditions and from the same initial conditions, differing only in this aspect (Table 1).

The effects of submesoscale baroclinic instability is parameterized as an overturning streamfunction (Fox-Kemper et al. 2008, 2011):

$$\Psi_o = \frac{\Delta s}{L_f} C_e \frac{H^2 \nabla_h b \times \hat{\boldsymbol{z}}}{|f|} \mu(z), \tag{1}$$

$$\mu(z) = \left[1 - \left(\frac{2z}{H} + 1\right)^2\right]\left[1 + \frac{5}{21}\left(\frac{2z}{H} + 1\right)^2\right], \tag{2}$$

where C_e is a constant set to 0.06, H is MLD as determined by a density difference from the surface, b is the buoyancy formed from the density ρ and background density ρ_0 by $b = g(\rho_0 - \rho)/\rho_0$, $\nabla_h b$ is the gridscale horizontal buoyancy gradient and the factor $\Delta s/L_f$ includes the horizontal grid scale and a frontal scaling factor that accounts for the coarse horizontal resolution of the model (Fox-Kemper et al. 2011). The typical effect of this parameterization is to shoal the mixed layer by overturning lateral fronts wherever they are present to increase the vertical stratification, at a rate consistent with simulations and observations of mixed layer eddy processes.

The Langmuir turbulence parameterization developed by Q. Li et al. (2016) accounts for the additional vertical boundary layer mixing that occurs when Stokes drift from surface waves (which is extracted from the WAVEWATCH III component model across the globe and depends on the winds and ocean currents of the other model components) interacts with near-surface boundary layer turbulence resulting in downward accelerations by a wave-current interaction called the Stokes shear force (Suzuki and Fox-Kemper 2016). The rate of additional mixing beyond wind-driven mixing is estimated in large-eddy simulations resolving Langmuir turbulence (Van Roekel et al. 2012) and included in KPP following the parameterization form suggested by McWilliams and Sullivan (2000). The parameterization mostly increases the vertical turbulent velocity scale within the boundary layer by an enhancement factor $\mathcal{E}$:

$$W = \frac{ku^*}{\phi} \rightarrow W = \frac{ku^*}{\phi}\mathcal{E}, \tag{3}$$

$$\mathcal{E} = |\cos\alpha|\sqrt{1 + (c_1 \mathrm{La})^{-2} + (c_2 \mathrm{La})^{-4}}. \tag{4}$$

The angle α is the predicted angle between the Langmuir cell orientation and the surface wind orientation, $c_1 = 1.5$, $c_2 = 5.4$ are dimensionless constants, and La is the surface layer-averaged, turbulent Langmuir number formed from projecting both the wind stress and Stokes drift into the Langmuir cell orientation (Van Roekel et al. 2012; Q. Li et al. 2016), or

$$\mathrm{La} = \sqrt{\frac{u^* \cos\alpha}{|\langle u_s \rangle| \cos(\theta_{ww} - \alpha)}}. \tag{5}$$

Here θ_{ww} is the angle between the wind and the wave direction, $\langle u_s \rangle$ is the Stokes drift averaged over the surface layer—i.e., the upper 20% of the mixed layer (Harcourt and D'Asaro 2008)—and α is found from application of the "law of the wall" as derived in Van Roekel et al. (2012). The additional effects of Langmuir mixing on entrainment at the mixed layer base (Li and Fox-Kemper 2017) were not used for this study.

In summary, the submesoscale restratification depends on the horizontal buoyancy gradient and MLD and acts to shoal the ML. Conversely, Langmuir turbulence depends on waves and wind direction and strength, and acts to deepen the mixed layer. The combinations of parameterizations and cases are outlined in Table 1. These parameterizations rely on different resolved variables and therefore have different temporal and geographical influences over the BOB and globally. It should be noted that both of these parameterizations are the default in CESM2 (Danabasoglu et al. 2020), so the sensitivity under

study is the effect of turning each of or both of them off. The "control" run includes both parameterizations. For this study, each model version listed in Table 1 was initialized identically for 30-yr runs.

For analysis of the MISO, the annual mean and first three harmonics of the precipitation fields were removed, so that only subseasonal precipitation anomaly variations were retained. Then, a zonal average of precipitation data between 12.5°S–20.5°N and 80.5°–90.5°E isolated the region of interest. This choice has the advantage of eliminating any topography from the analysis region.

c. EEOF analysis

EEOFs are an application of singular value decomposition (SVD) which treats the decomposed values as representations of the temporal and spatial variability of a dataset (Thomson and Emery 2001). This study uses zonally averaged daily precipitation anomalies as its input data. The following equation shows the archetypal SVD in matrix notation:

$$\mathbf{M} = \mathbf{USV}^{\mathrm{T}} \tag{6}$$

where **M** is a spatiotemporal dataset organized with rows and columns as spatial grid locations and time steps, **U** and **V** are its left and right singular vectors, and **S** is the matrix of singular values. The matrix **V** is a square matrix with the same dimensions as the spatial grid of the original data matrix and each of its columns is a normalized pattern or mode of spatial variability that repeats in the anomaly data. The different patterns are guaranteed to be orthogonal. The left matrix **U** is a square matrix the size of the number of time steps in the data matrix, and each of its columns captures the normalized time series of each corresponding spatial mode, respectively. The time series are also orthogonal. The matrix **S** is a diagonal matrix capturing the amplitude and relative importance of each mode, typically ordered from the largest amplitude to the smallest. Note that orthonormality of **U** and **V** implies that the sum of the diagonals of $\mathbf{S}^2$ equals that of the original data matrix times its transpose, indicating that the spatiotemporal variance explained by each mode is captured by the corresponding singular value squared. The fraction of the variance represented by a particular mode is captured by the corresponding diagonal element squared divided by the sum of the squares of all of the diagonal elements of **S**. Similarly, (6) implies that the original data can be reconstructed from **U**, **S**, **V**, or approximated by retaining only a limited number of modes with the largest entries on the diagonal of **S**.

A temporal extended EOF (EEOF) involves expanding the original **M** matrix by concatenating a duplicate of the dataset which is offset (or "lagged") in time. Thus, the lagged data follows the same form as (6) has for a dataset with more spatial grid points. By simultaneously performing EOF analysis on the same data from slightly different starting times, a mode in a temporal EEOF captures not a single spatial pattern, but a sequential pattern of two consecutive days of evolving features (Weare and Nasstrom 1982). Here, an EEOF with lags ranging from 1 to 16 days (17 total days) is used to recognize patterns in the short-term evolution of the precipitation—i.e., the range of time expected for the MISO development. Terminology for EOFs and EEOFs varies widely: EEOFs with a number indicating their relative importance in terms of the corresponding **S** entry (e.g., EEOF1, EEOF2) and the time series describing the evolving amplitude of each set of lagged patterns are called principal components again numbered by importance (e.g., PC1, PC2). If the **S** values are all distinct, then each EEOF and PC are unique and distinct.

Sampling errors introduced by the EEOF method are evaluated using the methodology of North et al. (1982), who defined an approximation for the error of the eigenvalue corresponding to one EEOF:

$$\delta\lambda_\alpha \approx \lambda_\alpha (2/N)^{1/2}, \tag{7}$$

where N is the number of time intervals represented in the data, λ_α is the αth eigenvalue, and $\delta\lambda_\alpha$ is its associated sampling error. Here, solving for the significance values $\mathbf{S}^2$ in terms of the EOF decomposition allows us to write the following:

$$\delta\mathbf{S}_\alpha^2 \approx \mathbf{S}_\alpha^2 (2/N)^{1/2} \tag{8}$$

assuming that the sum of the diagonal of $\mathbf{S}^2$ is constant in time, which is reasonable. North et al. (1982) also gave an approximate relationship between sampling error of eigenfunctions and eigenvalues:

$$\delta\Phi_\alpha \approx \frac{\delta\lambda_\alpha}{\Delta\lambda_\alpha}\Phi_{\alpha'}, \tag{9}$$

where $\Phi_{\alpha'}$ is the eigenfunction after the αth eigenfunction, $\delta\Phi_\alpha$ is the sampling error associated with the αth eigenfunction, and $\Delta\lambda_\alpha = \lambda_\alpha - \lambda_{\alpha'}$. Functionally, this means that the magnitude of the orthogonal function relative to its sampling error depends on the magnitude of the corresponding $\mathbf{S}^2$ value relative to its sampling error.

It is important to note that EOF analysis in general is purely empirical and lacks dynamical cause-and-effect (Dommenget and Latif 2002), so the decomposed modes may not have any physical significance unless independently shown to do so. EOFs may produce apparent order in data beyond what is present. EOF analysis is particularly troubling if the real modes of variability are not orthogonal in time or space. EOF analysis can also be confusing when representing propagating patterns (Fox-Kemper 2004), but the EEOF approach makes rapidly propagating patterns simple to describe with a single EEOF. In this case, the MISO is well understood to be a north–south phenomenon, making it more natural to apply an EEOF method than in the case of, for instance, a spatial dataset with no a priori assumptions about modes of variability. The method is not being used here to identify unseen patterns but to evaluate one already identified.

As shown by Suhas et al. (2013) the EEOFs produced in this manner agree with other indices of MISO variability. Figure 1 shows the variation in PC1 over a few positive and negative phases of EEOF1, and the corresponding zonal-mean precipitation over the region below. It is clear that the northward-propagating precipitation pattern is captured by the PC1 time series, and the EEOF spatial pattern of propagation similarly matches

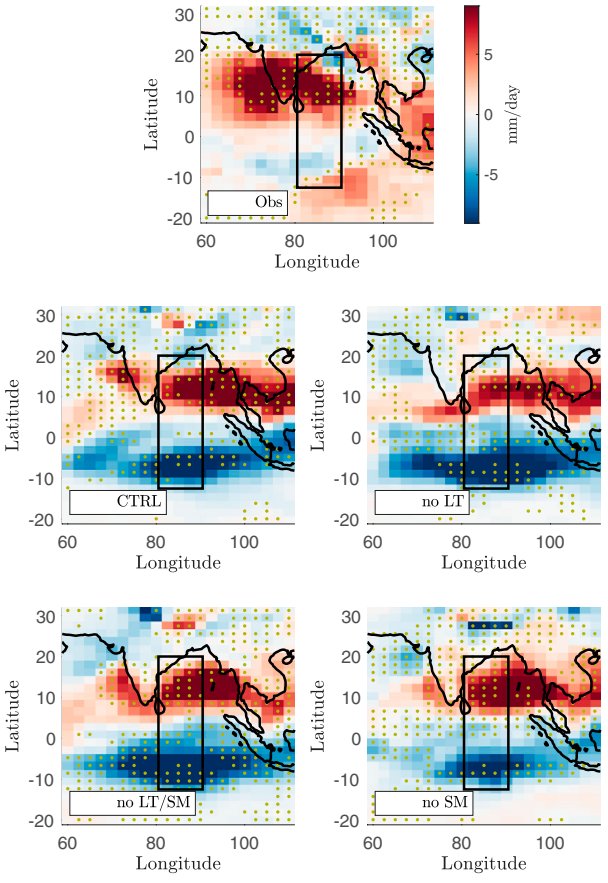

FIG. 2. Average difference in precipitation anomaly between positive and negative MISO1 phases. Maps show the difference between the average precipitation anomalies at all times for MISO1 > 95th percentile and all times for MISO1 < 5th percentile for (top) the observations (GPCP) and for the cases (Table 1): (middle) CTRL = both Langmuir and submesoscale and noLT = submesoscale only, and (bottom) noSM = Langmuir only and noLT/SM = neither parameterization. Color bar applies to all subfigures. Black boxes indicate the region used in the EEOF method. Yellow stippling indicates where the sign of change is not significant, i.e., where the inner 80% of a distribution of bootstrapped synthetic means is not purely positive or negative.

the precipitation propagation (not shown). Following Suhas et al. (2013), EEOF1 and EEOF2 are normalized by their standard deviations, and are hereafter referred to as MISO1 and MISO2. For the purposes of this work, MISO maxima and minima are identified here as peaks and troughs in MISO1 (delineated by the 5th and 95th percentiles over the whole record). Other EOF-based definitions are common, e.g., for evaluating the Madden–Julian oscillation (MJO) (such as Kim and North 1999) or other climate variability signals (Weiss et al. 2019). In this case, MISO1 isolates the primary north–south mode of oscillation.

d. Composite maps

Composite maps of the difference in regional rainfall anomaly between active and break phases of the MISO are a complementary metric to the MISO1 pattern once the maximum and minimum MISO stages are found (Fig. 2). While the EEOF is formulated based only on rainfall in the BOB, composite plots of these time periods show a wider region, illustrating how the MISO phases defined by the EEOF manifest in the Indian Ocean as a whole. Furthermore, the composite precipitation averages are not limited by orthogonality of spatial patterns, or the fact that the linear construction of the EEOFs ensures symmetries that may not be present: e.g., EEOF1 in a positive phase is exactly the same as the negative of EEOF1 in a negative phase. Figure 3 illustrates that the composites over positive and negative phases indeed differ in spatial pattern.

3. Results and discussion

Solely matching the time scale of simulated MISO phenomenon identified by the EEOF analysis to that previously observed for the MISO does not indicate a complete model success, but together with a good spatial structure of the EEOFs and the patterns of the composite maps (Fig. 2), alternative mechanisms become increasingly unlikely. The short lag interval (1–16 days) chosen for EEOF-based MISO detection is insufficient to cover a full repetition of a MISO event followed by another, but it does capture the characteristic northward trend of the precipitation maximum within an individual event (Fig. 1). This shows the advantage of the EEOF method, which immediately isolates northward-propagating behavior.

The composite maps (Fig. 2) of the difference in precipitation anomaly between MISO positive and negative phase peaks (MISO1 maxima and minima) show clear regions of strong variability throughout the BOB and the surrounding region. The GPCP data has a strong positive center stretching from the BOB across India to the Arabian Sea. Closer to the equator, there is a diffuse precipitation minimum during the MISO positive phase. These precipitation patterns are not an input to the detection algorithm for EEOF1, but are consistently correlated with it. The models do a fair job of capturing the BOB center of activity, but tend to either overestimate the precipitation anomaly over Indonesia or underestimate the precipitation anomaly over western India. None of them show a positive anomaly region stretching as far west as in the GPCP data. Conversely, in all of the models, the opposing precipitation anomaly near the equator is too strong compared to the observations. However, it can be noted that none of the model phase means have any significant spatial correlation with the observations: −0.00 for the CTRL run, −0.09 for noLT, 0.11 for noLT/SM, and 0.06 for noSM. 50.8% of the gridcell points in the CTRL run positive phase mean are different from the observations at a 5% significance level (meaning 49.2% are not), while 49.2% are for the negative phase. Similarly, for the noLT run the values are 44.0% different for the positive phase and 50.9% for the negative; for the noLT/SM run, 53.7% for the positive phase and 43.6% for the negative; and for the noSM run, 52.2% for the positive phase and 62.0% for the negative. By that measure, the most significant differences from the observations occur for the noSM run's negative phase mean and the noLT/SM run's positive phase mean, while

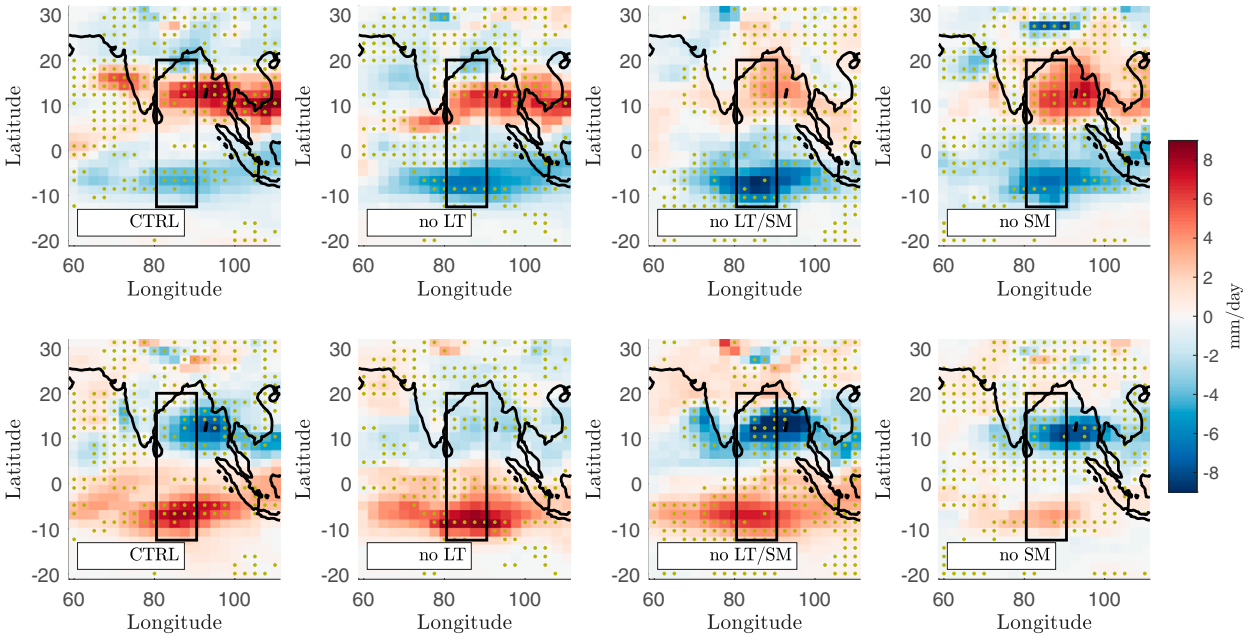

FIG. 3. Average positive and negative precipitation phases. Maps show the average precipitation anomalies at all times for (top) MISO1 > 95th percentile and (bottom) all times for MISO1 < 5th percentile. Shown are the cases (Table 1): CTRL = both Langmuir and submesoscale, noLT = submesoscale only, noLT/SM = neither parameterization, and noSM = Langmuir only. Color bar, black box, and stippling are as in Fig. 2.

the fewest significant differences occur for the noLT/SM run's negative phase mean and the noLT run's positive phase mean.

It is important to provide context to these phase maps by looking at the SST distribution of the model version. As shown in the left subfigure of Fig. 4, all four models have a slight cold bias in monsoon season average SST in the EEOF region. These data are further broken up in the right subfigure, which shows that all model versions but noSM have a negative bias in the difference between the North and South halves of the EEOF region. That gradient has been previously established (Samanta et al. 2018) and is supported by the observations used here.

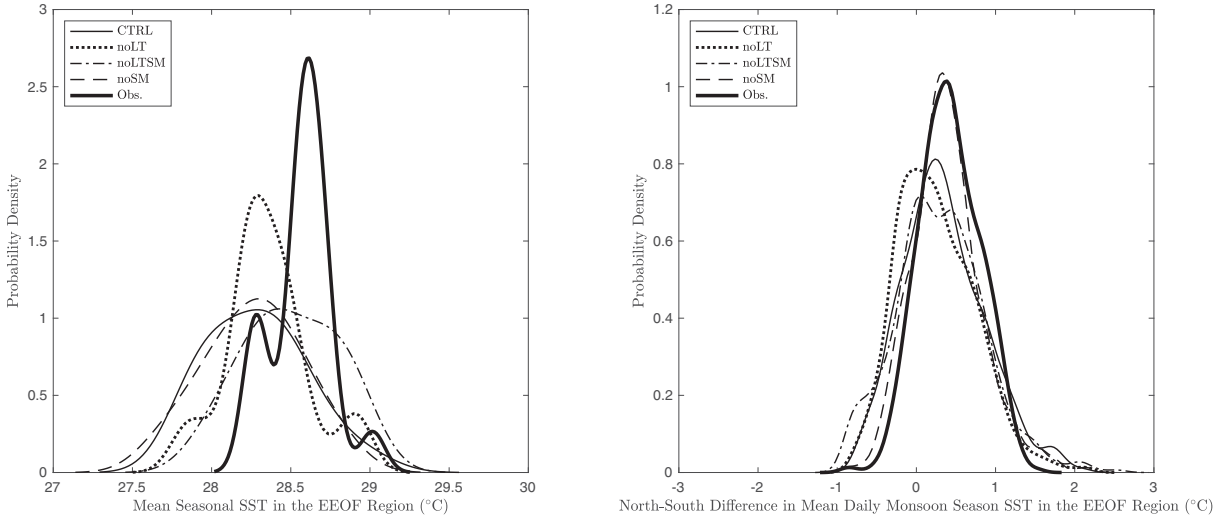

FIG. 4. Kernel density plots of monsoon season average SST in (left) the EEOF region and (right) daily temperature difference between the north and south components of the EEOF region. Observations are from the Group for High Resolution Sea Surface Temperature (GHRSST) global Level 4 sea surface temperature analysis of the National Centers for Environmental Information (NCEI) (Reynolds et al. 2007). Shown are the cases (Table 1): CTRL = both Langmuir and submesoscale, noLT = submesoscale only, noLTSM = neither parameterization, noSM = Langmuir only, and Obs = observations.

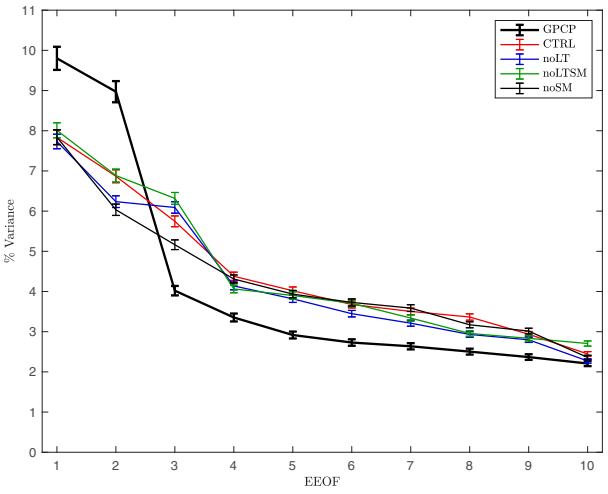

FIG. 5. Comparison of the relative importance of the first 10 EEOFs for GPCP observations and all model configurations. Method for calculating the percent of variance explained by each EEOF discussed in text. The first EEOF value corresponds to the percent variance represented by the MISO1 index. Shown are the cases (Table 1): GPCP = observations, CTRL = both Langmuir and submesoscale, noLT = submesoscale only, noLTSM = neither parameterization, and noSM = Langmuir only. Error bars calculated using the method of North et al. (1982) as discussed in text.

The EEOFs for all of the datasets have very broad singular value distributions, meaning the first few EEOFs account for only a modest portion of the variance which captures many other sources of precipitation variability. In GPCP, the first two EEOFs explain 9.80% and 8.97% of the total variance, respectively. For the CESM control run with both Langmuir and submesoscale turbulence, the first two EEOFs explain 7.83% and 6.87% of the variance. Removing Langmuir turbulence leaves 7.73% and 6.24%, while removing submesoscale turbulence gives a greater spread of 7.86% and 6.03%. Removing both gives 8.01% and 6.89% (Fig. 5). Thus, the MISO is stronger as a fraction of total precipitation variance in the real world than in the simulations, which tend to spread precipitation variance more evenly among modes. The sampling error calculated using Eq. 8 shows that the EEOFs are distinct through at least EEOF4 for all five datasets, with the exception of EEOF2 and EEOF3 for the noLT model run, which appear to be degenerate. This is consistent with the results of Suhas et al. (2013), in which only EEOF1 and EEOF2 passed that criteria. In other words, EEOF1 and EEOF2 of the CESM versions represent a smaller fraction of the total variance when compared to EEOF1 and EEOF2 of the observations, but since the precipitation variance in CESM is higher in $(\text{mm day}^{-1})^2$, the rainfall anomalies explained by EEOFs 1 and 2 of CESM matches that of the observations.

Active, or positive, MISO period identified in observations by the EEOF method have an average period of 31 days (Fig. 6 top row), which is consistent with previous descriptions of the MISO as approximately 30–60 days long (Goswami et al. 2016). This recurrence time exceeds the lag interval used to formulate the EEOF. The control model version exhibits the most similar behavior, with active periods on average 37 days long. The two model versions without Langmuir turbulence show the greatest difference from the observations: the noLT version has active phases on average 52 days long, while the noLTSM version has 123 days. This trend is similarly evident in the distribution of negative MISO phases (right column). Note the difference in sample size caused by the longer time span of the model runs. Additionally, it is important to note the limitations in looking at phase behavior introduced by the low model resolution. For instance, a 2.5° grid resolution can lead to large rainfall anomalies very close together or as far apart as 5 km being classified as in neighboring boxes in two model versions, which could possibly create significant artifacts of the grid itself.

Examining the model output data itself for ocean MLD sheds some light on the process-scale effects of the turbulence parameterizations. Figure 7 shows that while the CESM simulations including parameterizations of mixed layer eddies and Langmuir turbulence do have the most similar MISO statistics to the GPCP, the MLD in the BOB, and the north–south gradient of MLD differ significantly from an observations for this simulation, here drawn from Montégut et al. (2004). The definition of mixed layer used in CESM and in the observations is consistent, so the distinctions are not semantic. The observations exhibit a shallower average MLD than the CESM versions during almost the entire EEOF period, and much less annual variability. Furthermore, the version that performs best in reproducing the MISO (CTRL, solid line) does not have the MLD closest to observations. This comparison of MLDs indicates that 1) the CESM has room for improvement, and 2) under the coarse vertical resolution and numerics of the CESM a "good" MLD may not select for the best MISO variability, and 3) there are likely other model biases (e.g., clouds, precipitation, or atmospheric boundary layer parameterizations) that are providing additional errors beyond those being assessed here by altering the upper ocean parameterizations.

Alternatively, it is possible that it is changes to the mixed layer *outside* of the BOB that are having a beneficial effect on dynamics within the bay—an issue that cannot be addressed with the global model design used here. Furthermore, it is important to note that the model's fidelity in representing the MISO could be clouded by broader biases in reproducing the Indian monsoon as a whole. In particular, a connection involving the Bjerknes feedback has been shown to create a bias in rainfall and temperature which resembles, but does not actually constitute, a north–south dipole in the eastern Indian Ocean (G. Li et al. 2015, 2016). This finding also resembles our results in that it is associated with an unnaturally shallow summer MLD, which all four model versions show (Fig. 7). Thus, a variety of diagnostics, in addition to the method of Suhas et al. (2013) chosen here, are needed to fully assess the MISO and models' ability to predict it.

4. Conclusions

The EEOF method of Suhas et al. (2013) captures local modes of variability like the MISO. In this analysis, the MISO statistics

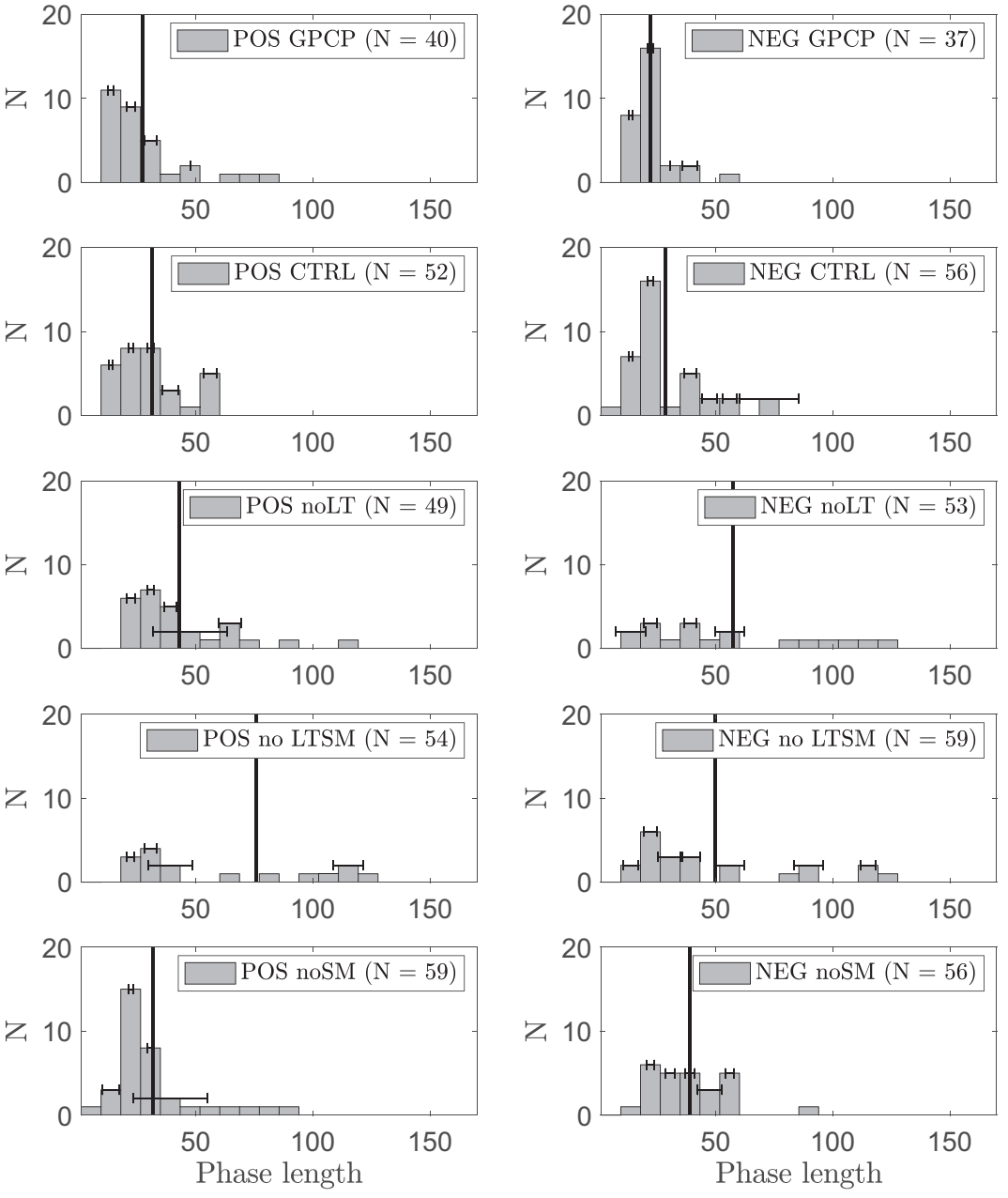

FIG. 6. Distribution of length in days of (left) positive and (right) negative phases of the MISO1 index for GPCP observations and all model configurations. Shown are the cases (Table 1): GPCP = observations, CTRL = both Langmuir and submesoscale, noLT = submesoscale only, noLTSM = neither parameterization, and noSM = Langmuir only. The number in the top-right corner of each subplot indicates the total number of phases represented in each distribution—note that the sample size is smaller for the observations (GPCP) since the time span of the data is shorter. The vertical line shows the mean value of each distribution. Horizontal whiskers show 95% confidence interval in the mean of each bin.

are significantly sensitive to upper ocean parameterizations, here Langmuir turbulence and mixed layer eddy parameterizations, even when all other aspects of the model are unchanged. Thus, upper ocean physics nontrivially impacts the MISO.

The upper ocean turbulence plays a large role in ocean–atmosphere interactions and the MISO is an inherently marine weather phenomena. However, most numerical weather prediction system analyses tend to focus on simulation of sea surface temperature, not MLD. The models here differ in both SST anomaly statistics and MLD, but these are not easily separated as both effects stem from substituting among self-consistent parameterizations. If solely the SST warming of submesoscale

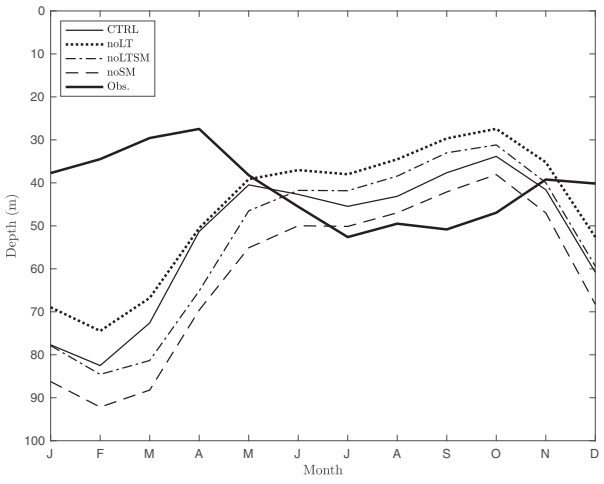

FIG. 7. Monthly climatology of spatially averaged MLD in the EEOF region from observations and for each model configuration. Observational dataset from Montégut et al. (2004). Shown are the cases (Table 1): CTRL = both Langmuir and submesoscale, noLT = submesoscale only, noLTSM = neither parameterization, noSM = Langmuir only, and Obs. = observations.

restratification was included without altering the MLD, it would not be physically meaningful.

The composite maps shown for CESM (Fig. 2) show that it is not only persistence of the MISO phenomena that is affected by upper ocean physics, but also the spatial patterns can be made more or less realistic. The effects near the equator, where all of the simulations have too little coherent precipitation with the positive MISO phase, indicates that there are likely other biases to address, e.g., the double ITCZ bias (Zhang et al. 2019).

Interestingly, the BOB MLDs of the model most successful in simulating the MISO are not the most accurate in comparison to observations. Thus, the mechanisms at play in the model to simulate the MISO are different than those in the real world—a fact that is not surprising given the complexity of the cloud formations in a real MISO (Kumar et al. 2017) versus the simplified MISO in the CESM. It is not at all clear if the model improvements shown here are a vindication of the particular set of parameterizations chosen, or just a coincidental set of factors combining into an improved MISO.

Methods like EEOF analysis can help identify such phenomena and define a rigorous way to extract targeted skill tests from observations and climate models in such a way that they can be directly compared. Measuring precipitation alone without the added perspective of the EEOF framework obscures the connection between upper ocean physics and the MISO, since upper ocean physics also affects other aspects of the precipitation patterns that conceal the MISO signature. On the other hand, EEOFs have the potential to spuriously indicate modes of oscillation where there may be none, so the spatial and temporal patterns must be evaluated critically as done here.

EOFs (and EEOFs) can also provide the basis for an empirical prediction system (Penland and Magorian 1993; Weiss et al. 2019) which can offer comparable forecast skill to full process-based modeling systems (Newman and Sardeshmukh 2017). Thus, the result here that upper ocean processes affect MISO EEOF statistics is likely to impart an impact on the potential forecast skill of process-based models.

The independence of EEOF analysis from model physics is both a strength and a weakness of the methodology. On the one hand, by making no assumptions about the dynamics of MISO events an EEOF can focus purely on their observed empirical behavior. Additionally, here we compound this agnosticism by using precipitation as our base variable, focusing on an effect of a MISO rather than a theorized mechanism. However, a more detailed look into the changing coupled air-sea mechanisms triggered by the different upper ocean physics is an important next step to better understand the nature of the sensitivity found here.

Comparing versions of a general circulation model (GCM) with and without various forms of turbulence has significant value from the perspective of climate mechanisms and model physics. Since the precipitation patterns associated with MISOs form in the Indian Ocean and move north through the BOB, this model comparison provides an opportunity to test how important ocean turbulence is to such synoptic scale phenomena. However, as the perturbed physics in this CESM ensemble was perturbed *globally*, it is not clear if the local effects on the upper BOB was the key change, or if other regions affected the initiation of the MISOs elsewhere, for example. The mismatch between model MISO accuracy and BOB MLDs would be natural if the improved skill descended from changes elsewhere rather than local changes. Using perturbed BOB physics in a regional climate model forced with identical remote forcing can distinguish between the impacts of local and remote physics, as can better understanding of the perturbed mechanisms underlying these changes to the MISO.

The importance of intraseasonal behavior to global climate predictions has become clear over the last decade. The most significant mode of East-West tropical intraseasonal variation, the MJO, has been shown in GCMs to nearly double in simulations with quadrupled atmospheric CO_2 levels. The precipitation anomalies associated with the MJO are projected to increase by 10% with every degree Celsius of surface temperature warming, partly due to increases in surface heat flux, but primarily due to a significant increase in vertical atmospheric circulation (Arnold et al. 2015). Since MISOs exhibit a similar mechanism, their response to climate change should be studied once a climate model is vetted for adequacy.

Overall, it is clear that the simulated MISO in this model is sensitive to upper ocean physics that contributes to mixed layer balances, not just prescribed MLDs (Samanta et al. 2018). Furthermore, in this particular model, the most realistic MISO did not occur in the model with the most accurate MLD, revealing that the whole of the model, including other inaccuracies, need to be taken into account when assessing forecast skill potential. By isolating propagating features in noisy data, the EEOF method arrived at this result in a way that is empirical, computationally inexpensive, and easy to reproduce.

Acknowledgments. BFK, LJ, and AS were funded by ONR N00014-17-1-2393. Computing was supported by NSF

1655221. Conversations with Eric D'Asaro, Amit Tandon, Jen MacKinnon, and others on the MISO-BoB team helped to focus this work. The Global Precipitation Climatology Project (GPCP) 1 Degree Daily product may be obtained at https://www.ncdc.noaa.gov/wdcmet/data-access-search-viewer-tools/global-precipitation-climatology-project-gpcp-clearinghouse. All CESM data used here are available on the Brown University digital repository (https://repository.library.brown.edu). The MLD climatology data (Montégut et al. 2004) may be accessed at http://www.ifremer.fr/cerweb/deboyer/mld/Surface_Mixed_Layer_Depth.php.

REFERENCES

Adler, R. F., and Coauthors, 2003: The Version-2 Global Precipitation Climatology Project (GPCP) monthly precipitation analysis (1979–present). *J. Hydrometeor.*, **4**, 1147–1167, https://doi.org/10.1175/1525-7541(2003)004<1147:TVGPCP>2.0.CO;2.

Akter, N., and K. Tsuboki, 2014: Role of synoptic-scale forcing in cyclogenesis over the Bay of Bengal. *Climate Dyn.*, **43**, 2651–2662, https://doi.org/10.1007/s00382-014-2077-9.

Anand, A., S. K. Mishra, S. Sahany, M. Bhowmick, J. S. Rawat, and S. K. Dash, 2018: Indian summer monsoon simulations: Usefulness of increasing horizontal resolution, manual tuning, and semi-automatic tuning in reducing present-day model biases. *Sci. Rep.*, **8**, 3522, https://doi.org/10.1038/s41598-018-21865-1.

Arnold, N. P., M. Branson, Z. Kuang, D. A. Randall, and E. Tziperman, 2015: MJO intensification with warming in the superparameterized CESM. *J. Climate*, **28**, 2706–2724, https://doi.org/10.1175/JCLI-D-14-00494.1.

Boccaletti, G., R. Ferrari, and B. Fox-Kemper, 2007: Mixed layer instabilities and restratification. *J. Phys. Oceanogr.*, **37**, 2228–2250, https://doi.org/10.1175/JPO3101.1.

Danabasoglu, G., and Coauthors, 2020: The Community Earth System Model version 2 (CESM2). *J. Adv. Model. Earth Syst.*, **12**, e2019MS001916, https://doi.org/10.1029/2019MS001916.

Dommenget, D., and M. Latif, 2002: A cautionary note on the interpretation of EOFs. *J. Climate*, **15**, 216–225, https://doi.org/10.1175/1520-0442(2002)015<0216:ACNOTI>2.0.CO;2.

Eshel, G., 2012: *Spatiotemporal Data Analysis.* Princeton University Press, 336 pp.

Fox-Kemper, B., 2004: Wind-driven barotropic gyre II: Effects of eddies and low interior viscosity. *J. Mar. Res.*, **62**, 195–232, https://doi.org/10.1357/002224004774201690.

——, R. Ferrari, and R. Hallberg, 2008: Parameterization of mixed layer eddies. Part I: Theory and diagnosis. *J. Phys. Oceanogr.*, **38**, 1145–1165, https://doi.org/10.1175/2007JPO3792.1.

——, and Coauthors, 2011: Parameterization of mixed layer eddies. III: Implementation and impact in global ocean climate simulations. *Ocean Modell.*, **39**, 61–78, https://doi.org/10.1016/j.ocemod.2010.09.002.

Goswami, B. N., and R. S. A. Mohan, 2001: Intraseasonal oscillations and interannual variability of the Indian summer monsoon. *J. Climate*, **14**, 1180–1198, https://doi.org/10.1175/1520-0442(2001)014<1180:IOAIVO>2.0.CO;2.

——, and P. K. Xavier, 2003: Potential predictability and extended range prediction of Indian summer monsoon breaks. *Geophys. Res. Lett.*, **30**, 1996, https://doi.org/10.1029/2003GL017810.

——, R. S. Ajayamohan, P. K. Xavier, and D. Sengupta, 2003: Clustering of synoptic activity by Indian summer monsoon intraseasonal oscillations. *Geophys. Res. Lett.*, **30**, 1431, https://doi.org/10.1029/2002GL016734.

——, S. A. Rao, D. Sengupta, and S. Chakravorty, 2016: Monsoons to mixing in the Bay of Bengal: Multiscale air-sea interactions and monsoon predictability. *Oceanography*, **29**, 18–27, https://doi.org/10.5670/oceanog.2016.35.

Harcourt, R. R., and E. A. D'Asaro, 2008: Large-eddy simulation of Langmuir turbulence in pure wind seas. *J. Phys. Oceanogr.*, **38**, 1542–1562, https://doi.org/10.1175/2007JPO3842.1.

Huffman, G. J., and Coauthors, 1997: The Global Precipitation Climatology Project (GPCP) combined precipitation dataset. *Bull. Amer. Meteor. Soc.*, **78**, 5–20, https://doi.org/10.1175/1520-0477(1997)078<0005:TGPCPG>2.0.CO;2.

——, R. F. Adler, D. T. Bolvin, and G. Gu, 2009: Improving the global precipitation record: GPCP version 2.1. *Geophys. Res. Lett.*, **36**, L17808, https://doi.org/10.1029/2009GL040000.

Hurrell, J. W., and Coauthors, 2013: The Community Earth System Model: A framework for collaborative research. *Bull. Amer. Meteor. Soc.*, **94**, 1339–1360, https://doi.org/10.1175/BAMS-D-12-00121.1.

Kim, K.-Y., and G. R. North, 1999: EOF-based linear prediction algorithm: Examples. *J. Climate*, **12**, 2076–2092, https://doi.org/10.1175/1520-0442(1999)012<2076:EBLPAE>2.0.CO;2.

Krishnamurthy, V., and J. Shukla, 2000: Intraseasonal and interannual variability of rainfall over India. *J. Climate*, **13**, 4366–4377, https://doi.org/10.1175/1520-0442(2000)013<0001:IAIVOR>2.0.CO;2.

Krishnamurti, T. N., and P. Ardanuy, 1980: The 10 to 20-day westward propagating mode and "breaks in the monsoons." *Tellus*, **32**, 15–26, https://doi.org/10.1111/j.2153-3490.1980.tb01717.x.

Kumar, S., A. Arora, R. Chattopadhyay, A. Hazra, S. A. Rao, and B. Goswami, 2017: Seminal role of stratiform clouds in large-scale aggregation of tropical rain in boreal summer monsoon intraseasonal oscillations. *Climate Dyn.*, **48**, 999–1015, https://doi.org/10.1007/s00382-016-3124-5.

Kuppam, A. P., and M. Mawsynram, 2019: The South Asian monsoon, past, present and future: A story of famines and trade, science and cupidity. *The Economist*, https://www.economist.com/essay/2019/06/27/the-south-asian-monsoon-past-present-and-future.

Langmuir, I., 1938: Surface motion of water induced by wind. *Science*, **87**, 119–123, https://doi.org/10.1126/science.87.2250.119.

Large, W. G., J. C. McWilliams, and S. C. Doney, 1994: Oceanic vertical mixing: A review and a model with a nonlocal boundary layer parameterization. *Rev. Geophys.*, **32**, 363–403, https://doi.org/10.1029/94RG01872.

Leibovich, S., 1983: The form and dynamics of Langmuir circulations. *Annu. Rev. Fluid Mech.*, **15**, 391–427, https://doi.org/10.1146/annurev.fl.15.010183.002135.

Li, G., S.-P. Xie, and Y. Du, 2015: Monsoon-induced biases of climate models over the tropical Indian Ocean. *J. Climate*, **28**, 3058–3072, https://doi.org/10.1175/JCLI-D-14-00740.1.

——, ——, and Y. Du, 2016: A robust but spurious pattern of climate change in model projections over the tropical Indian Ocean. *J. Climate*, **29**, 5589–5608, https://doi.org/10.1175/JCLI-D-15-0565.1.

Li, Q., and B. Fox-Kemper, 2017: Assessing the effects of Langmuir turbulence on the entrainment buoyancy flux in the ocean surface boundary layer. *J. Phys. Oceanogr.*, **47**, 2863–2886, https://doi.org/10.1175/JPO-D-17-0085.1.

——, A. Webb, B. Fox-Kemper, A. Craig, G. Danabasoglu, W. G. Large, and M. Vertenstein, 2016: Langmuir mixing effects on global climate: WAVEWATCH III in CESM.

Ocean Modell., **103**, 145–160, https://doi.org/10.1016/j.ocemod.2015.07.020.

——, and Coauthors, 2019: Comparing ocean surface boundary vertical mixing schemes including Langmuir turbulence. *J. Adv. Model. Earth Syst.*, **11**, 3545–3592, https://doi.org/10.1029/2019MS001810.

Li, Y., W. Han, W. Wang, and M. Ravichandran, 2016: Intraseasonal variability of SST and precipitation in the Arabian Sea during the Indian summer monsoon: Impact of ocean mixed layer depth. *J. Climate*, **29**, 7889–7910, https://doi.org/10.1175/JCLI-D-16-0238.1.

——, ——, W. Wang, L. Zhang, and M. Ravichandran, 2018: The Indian summer monsoon intraseasonal oscillations in CFSv2 forecasts: Biases and importance of improving air–sea interaction processes. *J. Climate*, **31**, 5351–5370, https://doi.org/10.1175/JCLI-D-17-0623.1.

MacKinnon, J. A., and Coauthors, 2016: A tale of two spicy seas. *Oceanography*, **29**, 50–61, https://doi.org/10.5670/oceanog.2016.38.

McWilliams, J. C., and P. P. Sullivan, 2000: Vertical mixing by Langmuir circulations. *Spill Sci. Technol. Bull.*, **6**, 225–237, https://doi.org/10.1016/S1353-2561(01)00041-X.

——, ——, and C.-H. Moeng, 1997: Langmuir turbulence in the ocean. *J. Fluid Mech.*, **334**, 1–30, https://doi.org/10.1017/S0022112096004375.

Mo, K. C., 2001: Adaptive filtering and prediction of intraseasonal oscillations. *Mon. Wea. Rev.*, **129**, 802–817, https://doi.org/10.1175/1520-0493(2001)129<0802:AFAPOI>2.0.CO;2.

Montégut, C. B., G. Madec, A. S. Fischer, A. Lazar, and D. Iudicone, 2004: Mixed layer depth over the global ocean: An examination of profile data and a profile based climatology. *J. Geophys. Res.*, **109**, C12003, https://doi.org/10.1029/2004JC002378.

Newman, M., and P. D. Sardeshmukh, 2017: Are we near the predictability limit of tropical Indo-Pacific sea surface temperatures? *Geophys. Res. Lett.*, **44**, 8520–8529, https://doi.org/10.1002/2017GL074088.

North, G. R., T. L. Bell, R. F. Cahalan, and F. J. Moeng, 1982: Sampling errors in the estimation of empirical orthogonal functions. *Mon. Wea. Rev.*, **110**, 699–706, https://doi.org/10.1175/1520-0493(1982)110<0699:SEITEO>2.0.CO;2.

Pattanaik, D. R., and Coauthors, 2012: Monthly forecast of Indian southwest monsoon rainfall based on NCEP's coupled forecast system. *Atmos. Climate Sci.*, **2**, 479, https://doi.org/10.4236/acs.2012.24042.

Penland, C., and T. Magorian, 1993: Prediction of Niño-3 sea surface temperatures using linear inverse modeling. *J. Climate*, **6**, 1067–1076, https://doi.org/10.1175/1520-0442(1993)006<1067:PONSST>2.0.CO;2.

Ramachandran, S., and Coauthors, 2018: Submesoscale processes at shallow salinity fronts in the Bay of Bengal: Observations during the winter monsoon. *J. Phys. Oceanogr.*, **48**, 479–509, https://doi.org/10.1175/JPO-D-16-0283.1.

Reynolds, R. W., T. M. Smith, C. Liu, D. B. Chelton, K. S. Casey, and M. G. Schlax, 2007: Daily high-resolution-blended analyses for sea surface temperature. *J. Climate*, **20**, 5473–5496, https://doi.org/10.1175/2007JCLI1824.1.

Samanta, D., S. N. Hameed, D. Jin, V. Thilakan, M. Ganai, S. A. Rao, and M. Deshpande, 2018: Impact of a narrow Coastal Bay of Bengal sea surface temperature front on an Indian summer monsoon simulation. *Sci. Rep.*, **8**, 17694, https://doi.org/10.1038/s41598-018-35735-3.

Sarkar, S., H. Pham, S. Ramachandran, J. Nash, A. Tandon, J. Buckley, A. Lotliker, and M. Omand, 2016: The interplay between submesoscale instabilities and turbulence in the surface layer of the Bay of Bengal. *Oceanography*, **29**, 146–157, https://doi.org/10.5670/oceanog.2016.47.

Sengupta, D., B. N. Goswami, and R. Senan, 2001: Coherent intraseasonal oscillations of ocean and atmosphere during the Asian Summer Monsoon. *Geophys. Res. Lett.*, **28**, 4127–4130, https://doi.org/10.1029/2001GL013587.

Spiro Jaeger, G., and A. Mahadevan, 2018: Submesoscale-selective compensation of fronts in a salinity-stratified ocean. *Sci. Adv.*, **4**, e1701504, https://doi.org/10.1126/sciadv.1701504.

Suhas, E., J. M. Neena, and B. N. Goswami, 2013: An Indian Monsoon Intraseasonal Oscillations (MISO) index for real time monitoring and forecast verification. *Climate Dyn.*, **40**, 2605–2616, https://doi.org/10.1007/s00382-012-1462-5.

Suzuki, N., and B. Fox-Kemper, 2016: Understanding Stokes forces in the wave-averaged equations. *J. Geophys. Res. Oceans*, **121**, 3579–3596, https://doi.org/10.1002/2015JC011566.

Thomson, R. E., and W. J. Emery, 2001: *Data Analysis Methods in Physical Oceanography*. 2nd ed. Elsevier Science, 729 pp.

Van Roekel, L., B. Fox-Kemper, P. Sullivan, P. Hamlington, and S. Haney, 2012: The form and orientation of Langmuir cells for misaligned winds and waves. *J. Geophys. Res.*, **117**, C05001, https://doi.org/10.1029/2011JC007516.

Weare, B. C., and J. S. Nasstrom, 1982: Examples of extended empirical orthogonal function analyses. *Mon. Wea. Rev.*, **110**, 481–485, https://doi.org/10.1175/1520-0493(1982)110<0481:EOEEOF>2.0.CO;2.

Weiss, J. B., B. Fox-Kemper, D. Mandal, A. D. Nelson, and R. K. Zia, 2019: Nonequilibrium oscillations, probability angular momentum, and the climate system. *J. Stat. Phys.*, **179**, 1–18, https://doi.org/10.1007/s10955-019-02394-1.

Zhang, G. J., X. Song, and Y. Wang, 2019: The double ITCZ syndrome in GCMS: A coupled feedback problem among convection, clouds, atmospheric and ocean circulations. *Atmos. Res.*, **229**, 255–268, https://doi.org/10.1016/j.atmosres.2019.06.023.

Zhang, L., W. Han, Y. Li, and E. D. Maloney, 2018: Role of North Indian Ocean air–sea interaction in summer monsoon intraseasonal oscillation. *J. Climate*, **31**, 7885–7908, https://doi.org/10.1175/JCLI-D-17-0691.1.